JOURNAL OF GEOPHYSICAL RESEARCH, VOL. 106, NO. E10, PAGES 23,723–23,735, OCTOBER 25, 2001

Statistics of Mars' topography from the Mars Orbiter Laser Altimeter: Slopes, correlations, and physical Models

Oded Aharonson, Maria T. Zuber,[1] and Daniel H. Rothman

Department of Earth, Atmospheric and Planetary Sciences, Massachusetts Institute of Technology, Cambridge, Massachusetts

Abstract. Data obtained recently by the Mars Orbiter Laser Altimeter (MOLA) were used to study the statistical properties of the topography and slopes on Mars. We find that the hemispheric dichotomy, manifested as an elevation difference, can be described by long baseline tilts but in places is expressed as steeper slopes. The bimodal hypsometry of elevations on Mars becomes unimodal when referenced to the center of figure, contrary to the Earth, for which the bimodality is retained. However, ruling out a model in which the elevation difference is expressed in a narrow equatorial topographic step cannot be done by the hypsometry alone. Mars' slope distribution is longer tailed than those of Earth and Venus, indicating a lower efficiency of planation processes relative to relief-building tectonics and volcanics. We define and compute global maps of statistical estimators, including the interquartile scale, RMS and median slope, and characteristic decorrelation length of the surface. A correspondence between these parameters and geologic units on Mars is inferred. Surface smoothness is distinctive in the vast northern hemisphere plains, where slopes are typically $<0.5°$. Amazonis Planitia exhibits a variation in topography of <1 m over 35-km baselines. The region of hematite mineralization in Sinus Meridiani is also smooth, with median slopes lower than 0.4°, but does not form a closed basin. The shallower long-wavelength portion of the lowlands' topographic power spectrum relative to the highlands' can be accounted for by a simple model of sedimentation such as might be expected at an ocean's floor. The addition of another process such as cratering is necessary to explain the spectral slope in short wavelengths. Among their application, these MOLA-derived roughness measurements can help characterize sites for landing missions.

1. Introduction

As descriptors of planetary surfaces, slopes and slope distributions are pertinent to the mechanisms of formation of physiographic features and are indicative of the style and duration of subsequent modificational processes [e.g., *Scheidegger*, 1991]. As a step toward quantifying the nature of surface processes of Mars, we analyze elevation and slope statistics derived from profiles collected by the Mars Orbiter Laser Altimeter (MOLA) [*Zuber et al.*, 1992], an instrument on the Mars Global Surveyor (MGS) spacecraft. Since the origin of some large- and small-scale surface features remains in debate, the task of interpreting statistical models for geophysical information is ambiguous. Nonetheless, such statistical estimation can be useful, especially in a comparative sense and when additional observation types are included in the interpretation. For example, the topography of the Earth's seafloor has been characterized in detail by several studies [*Fox and Hayes*, 1985; *Goff and Jordan*, 1988; *Neumann and Forsyth*, 1995; *Smith and Jordan*, 1988] in terms of models describing its statistical properties and power spectrum, and several processes have been modeled with these tools, including seafloor spreading, sedimentation, and seamount distribution. The statistics of continental topography has been studied in landscapes such as eroding environments and river networks [e.g., *Rodríguez-Iturbe and Rinaldo*, 1997; *Scheiddeger*, 1991]. The stereographically derived topographic field of Mars that predated MGS [*Wu*, 1991; *Esposito et al.*, 1992] permitted only coarse study owing to its low precision and resolution. With the newly obtained information, an accurate statistical characterization is finally possible. Results based on initial data collected in the northern hemisphere were reported on by *Aharonson et al.* [1998] and more globally by *Aharonson et al.* [1999], *Kreslavsky and Head* [1999] and *Kreslavsky and Head* [2000].

2. Data Collection and Accuracy

The data set on which the following analysis is based was collected during the aerobreaking hiatus, science-phasing, and ongoing mapping orbits of Mars Global Surveyor [*Albee et al.*, 1998, this issue]. The data provide coverage of

[1] Also at Laboratory for Terrestrial Physics, NASA Goddard Space Flight Center, Greenbelt, Maryland.

Paper number 2000JE001403.
0148-0227/01/2000JE001403$09.00

the surface of Mars at 300- to 400-m spacing along track as dictated from the spacecraft orbital velocity and the laser pulse repetition frequency of 10 Hz. The MOLA instrument has a range resolution of 37.5 cm, a range precision of 1-10 m for surface slopes of up to 30°, and an absolute accuracy of ~1 m with respect to Mars' center of mass [*Zuber et al.*, 1992; *Neumann et al.*, this issue]. These data currently constitute the highest-quality measurements of Mars topography and permit quantification of slopes from local to hemispheric scale [*Smith et al.*, 1999, this issue]. The accuracy of point-to-point slopes along track is <0.1°. Resolving steep slopes is limited by the instrument's detection of reflected power, but this is rarely encountered, and only at slopes >45°. In the following sections, various statistical estimators will be defined and applied to the data set. A global view of elevations and slopes is presented first, followed by regional slope and power spectral characteristics.

3. Global Hypsometry

The most striking global feature of the surface of Mars is the crustal dichotomy. The northern hemisphere is topographically lower, morphologically smoother, and geologically younger than the south [*Carr*, 1981; *Mutch et al.*, 1976]. A frequency diagram of elevations, or hypsogram (Figure 1a), shows this dichotomy clearly, as was previously observed [e.g., *Smith and Zuber*, 1996; *Smith et al.*, 1999]. The strong bimodal distribution shows that the lowlands peak is ~5.5 km lower than the highlands and is narrower, indicating the flatness of the north. The distribution's lowest portion, the peak between −7 km and −6 km, is the floor of the Hellas impact basin in the south. *Sharpton and Head* [1985] and *Sharpton and Head* [1986] compared the topography and slopes of Earth and Venus. Using the same bin widths, the hypsometry of Mars has a larger overall range of elevations than Earth (and Venus) and is bimodal, appearing similar to Earth, as shown in Figure 1c [*National Geophysical Data Center*, 1988]. However, as shown by *Smith et al.* [1999] and by the solid black curves, by removing the spherical harmonic degree 1 terms, effectively referencing the topography to the geometric center of figure (COF) instead of the center of mass (COM), the distribution of topography of Mars becomes unimodal (as for Venus), whereas Earth maintains its bimodality.

It is instructive to consider a theoretical planet whose topography consists of an equatorial scarp of height 6 km with 1 km of normally distributed noise superimposed. Figure 1b shows the corresponding distributions of this "noisy cliff" model. Referencing to the COF also collapses the two sharp peaks of this model into one, but depending on the amount of noise, shoulders can remain in the histogram. We therefore conclude that the elevation histogram of Mars is consistent with the dichotomy having a global effect, but an

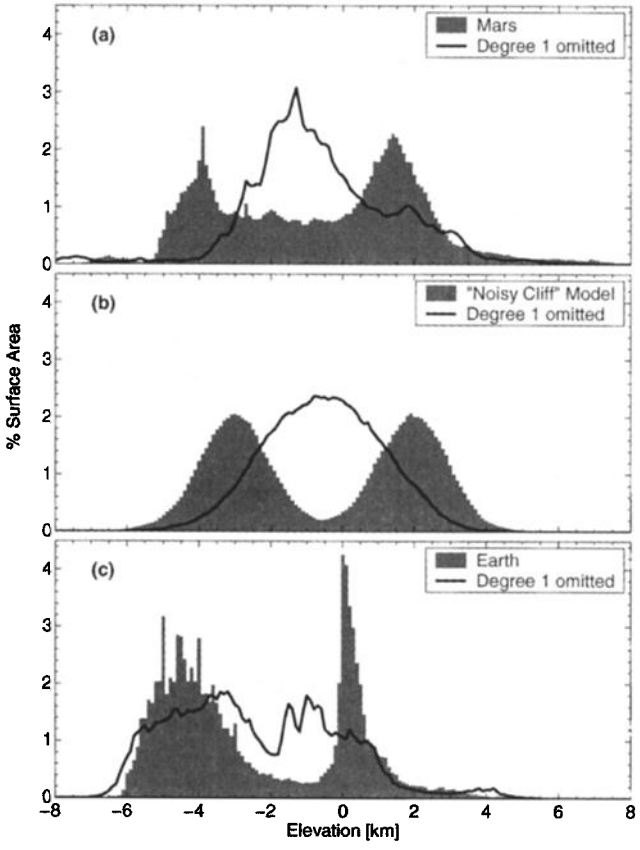

Figure 1. Hypsometry of surface topography from gridded elevation models. Bin width is 100 m. To compute an area weighted histogram, an equal-area projection of the data was used. The black curve is the elevation histogram with respect to the geoid, and the gray filled area is the distribution with the degree 1 terms removed. The distributions shown are for (a) Mars, (b) a synthetic "noisy cliff model," and (c) Earth.

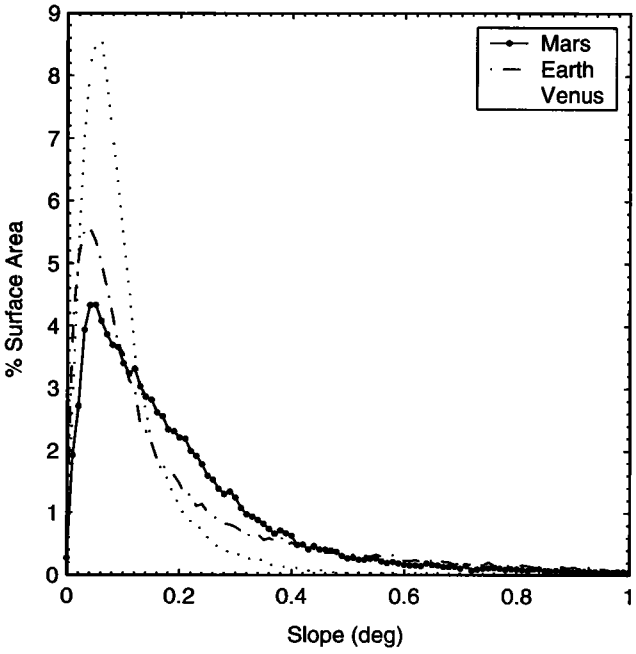

Figure 2. A histogram of regional slopes for Mars (solid curve), Earth (dashed), and Venus (dotted). Baselines for slope calculations were 100 km, and bin width is 0.01°, similar to *Sharpton and Head* [1985]. Note the relative abundance of steeper slopes in the range 0.18-0.42° on Mars.

equatorial scarp is not ruled out by the hypsometry alone. Additional analysis is required to isolate contributions to the hemispheric elevation difference, for example, by crustal thickness variations, as done by *Zuber et al.* [2000].

It is also possible to compare regional slopes on Mars to *Sharpton and Head* [1985] results for Earth and Venus. Figure 2 shows an equal area histogram of 100-km slopes binned in 0.01° bins. Similar to Venus, the distribution for Mars peaks near 0.05° but is longer tailed. In fact, on Venus, regional slopes rarely exceed 0.3°. The steeper slopes on Mars are presumably related to the lower efficiency of planation processes (which on Earth are often driven by the hydrosphere and atmosphere). However, the expected value of the absolute slope varies greatly by region and will be discussed in later sections.

4. Long-Baseline Tilts

Several studies have demonstrated that Mars' topography is characterized by a hemispherical-scale tilt. For example, *Smith et al.* [1999] and *Zuber et al.* [2000] observed that in a longitude band near the Mars prime meridian, the pole-to-pole topography can be described to first order by a pole-to-pole slope of ~0.036° downhill to the north. In addition *Phillips et al.* [2001], consider planetary-scale slopes due to Tharsis. To quantify long-baseline slopes on Mars, we gloablly compute slopes on 1000-km baselines by fitting planes of that dimension to locally projected gridded fields. The MOLA-derived topographic field has an absolute accuracy of ~1 m with respect to Mars' center of mass. Even allowing for errors in the height of the geoid of ~5 m [*Lemoine et al.*, this issue], 1000-km surface slopes have precision of better than $\sim 2° \times 10^{-5}$. Plate 1 shows the magnitude (color-coded) and direction (arrows) of these regional slopes. It is clear that the majority of the northern hemisphere slopes downward to the north. The lowlands have a typical tilt of 0.02-0.1° with values increasing to 0.4° near the dichotomy boundary in longitudes 50-210°E and the large volcanos. The basin floor of Hellas (44.3°S, 66.2°E) has an overall easterly tilt, although locally it has some northerly slopes. However, the basin's topography has been significantly altered since its formation [*Wichman and Schultz*, 1989; *Tanaka and Leonard*, 1995], so it is difficult to ascertain its primordial shape. The floor of the Utopia basin (47.6°N, 82.7°E) shows no discernible nonradial tilts by this method and attempts to reproduce the northerly tilt result of *McGill* [2001] where unsuccessful. Naturally, the north polar cap is tilted approximately south, while the south cap is tilted north, giving a quasi-parabolic shape which is consistent with ablation [*Zwally et al.*, 2000] and glacial flow [*Zuber et al.*, 1998a, b] models.

Arabia Terra (~30°N, 30°E) is broadly tilted by 0.05°-1.5° to the north-west, a direction to which many of the channels in the region closely adhere. This correspondence is also true in the area of Chryse (27°N, 324°E), although the slopes are ~0.05° steeper. The correlation between channel direction and gradient azimuth as a function of scale of the local slope is an exciting research direction presently being pursued in greater detail. It is notable here that channels are often oriented in a direction consistent with long-baseline slopes.

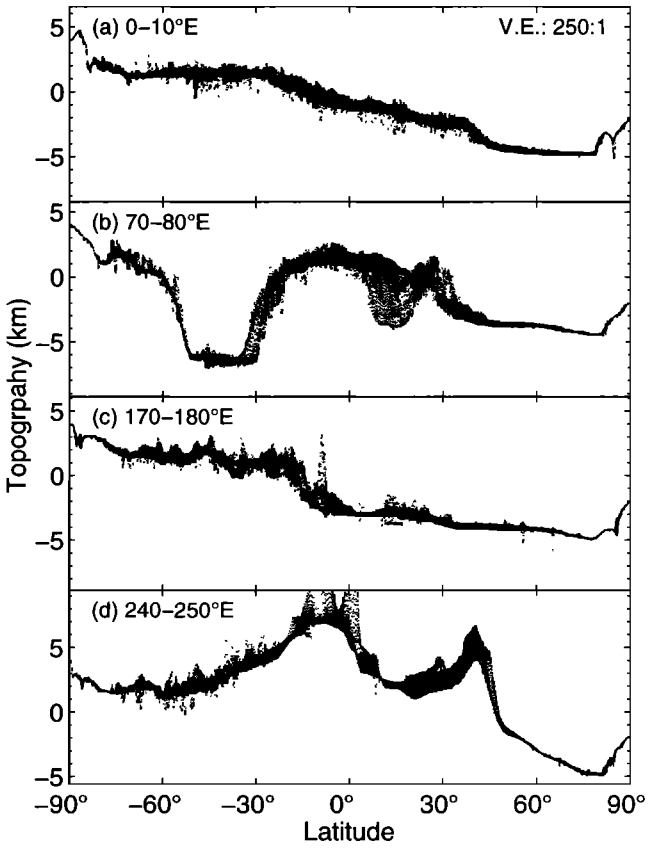

Figure 3. Pole-to-pole topographic profiles stacked in selected 10° longitude intervals.

Regional trends were also used in an analysis by *Mouginis-Mark et al.* [1982], where slope azimuths were compared to flow directions of Tharsis lava flows, which were taken as paleoslope indicators. They found almost no deformation associated with loading since the flow emplacement. The more precise slopes computed here are similar to the ones they used and therefore confirm their conclusion that during the current epoch of preserved volcanic activity the lithospheric thickness must be large (perhaps >150 km). This scenario is consistent with the thick elastic lithosphere determined from gravity and topography inversions of *Zuber et al.* [2000].

The orientation of the long-baseline slopes in the southern hemisphere is complicated by large impact and volcanic constructs such as Hellas, Argyre, and Tharsis (Figures 3b and 3d, Plate 1). At regions distant from these features, for example, near longitudes 0° and 170°-180°E (Figures 3a and 3c, Plate 1) slopes appear to be biased toward the north. Still other longitude bands (e.g., ~130°E, 200°-210°E) have random distribution of slope azimuths. The computed slopes indicate that a substantial fraction of the planet is tilted roughly northward, altough important departures from that exist, for instance, near Tharsis and Hellas. This supports the long-held view that the majority of the surface of Mars drains

north [*Banerdt and Vidal*, 2001], and that the lowlands are a natural sink for not only volatiles but also sedimentary, aeolian and volcanic materials [*Smith et al.*, this issue]. Although a description of long-baseline slopes is provided by the method presented, the question of possible global tilts remains open and attractive to further investigation using the highly precise MOLA data set.

5. RMS and Median Slope

Short-wavelength slopes are relevant to regional-scale processes on Mars. In order to investigate short-baseline slopes, MOLA tracks were numerically differentiated by a three-point Lagrange formula,

$$\frac{dy}{dx} = y_0 \frac{2x - x_1 - x_2}{x_{01}x_{02}} + y_1 \frac{2x - x_0 - x_2}{x_{10}x_{12}} + y_2 \frac{2x - x_0 - x_1}{x_{20}x_{21}}, \quad (1)$$

for three consecutive points at $\{(x_i, y_i)\}$ with $i = \{0, 1, 2\}$ and $x_{ij} = x_i - x_j$. For equally spaced points this is equivalent to a centered difference scheme. Formally, the result should be viewed as a lower limit on the absolute slope since the measurement is restricted to the ground-track direction, which may not follow the gradient direction. If the topography field is isotropic, the average properties that follow can easily be corrected for this by dividing by the average value of $|\cos(\theta)|$, that is, $2/\pi$.

It is customary to express surface roughness in terms of the root mean squares (RMS) of slopes θ_r, because radar reflection scatter is largely affected by this parameter. However, a typical slope distribution need not, and in fact rarely does, resemble a Gaussian, which is the distribution for which RMS is the appropriate measure. Point-to-point MOLA slopes can be anomalously large (e.g. owing to small craters or faults) and contribute to a long-tailed distribution. The L2 RMS slope estimate is sometimes dominated by these high slopes and is therefore not always representative of the typical nature of the surface [*Neumann and Forsyth*, 1995; *Kreslavsky and Head*, 1999].

Nonetheless, empirical study shows a surprising agreement between some RMS slope estimates derived from radar observations and from MOLA [*Aharonson et al.*, 1999]. Hence RMS slopes are reported here, but with a cautionary note, especially when these values are high.

RMS slopes were computed in a 35-km running window. The approximately hemispheric crustal dichotomy is manifested, with the southern hemisphere having typical RMS slopes in the range 3°-10° and the northern hemisphere in the range 0.2°-0.8° [*Head et al.*, 1999]. Exceptions to low slopes in the north include the Olympus Mons (18.4°N, 226.9°E) basal escarpment, canyon walls, sparse craters, and the edges of the ice cap deposits, while in the south low slopes are evident in the relatively flat portions of the ice cap deposits.

Radar observations of Mars [*Harmon et al.*, 1999; *Christensen*, 1986; *Christensen and Moore*, 1992] yield values for θ_r in the range 0.25°-10°, very similar to the overall range obtained here. The Tharsis Montes and Olympus Mons areas exhibit relatively high θ_r of ~10° in radar, and the MOLA data agree well. The Amazonian region west of Tharsis (16°N, 201°E) has large θ_r in radar but appears remarkably smooth in MOLA data. This indicates that although this region appears very smooth at MOLA scale, it may be rougher at a smaller scale. Chryse Planitia (27°N, 324°E), whose radar appearance played a role in site selection for Viking Lander 1, has θ_r of 4°-6° in radar and similarly in MOLA in the southern portion with values decreasing to ~1° in intercrater plains to the north. Syrtis Major at 10°N, 70°E has been observed to have some of the lowest effective θ_r in radar of ~1° down to 0°.25 and shows a slightly larger RMS slope by MOLA. This is an example of a surface that is probably smoother on a scale smaller than MOLA sampling than the point-to-point slopes would imply. Finally, the north polar region has a uniform radar response of θ_r ~2°, in fair agreement with MOLA.

In characterizing typical surface gradients, median absolute slopes were found to be most robust in that adjacent or crossing tracks show similar values. While RMS slopes suffer when distributions are long tailed owing to the averaging of squares of slopes, median absolute slopes are largely unaffected by the height of the distribution's tail [*Kreslavsky and Head*, 1999]. Plate 2 shows maps of median slopes in the same format as before.

A comparison with RMS slopes indicates that the median slope values are generally smaller, consistent with the remarks stated previously that a small amount of steep slopes can dominate the RMS measure. It is observed that median slopes contrast surfaces distinctly, so that, for example, the dune-covered Olympia Planitia (82°N, 166°E) appears slightly rougher than the north polar cap margins. Impact basins floor and rim characteristics emerge prominently. The large craters have a common morphology in which the floors are generally smoother than the rims and associated ejecta blankets. An interesting boundary in roughness occurs at the northern margin of the Tharsis province, approximately concentric with Alba Patera (40.5°N, 250.1°E) but ~1200 km north of its center. Median slope values drop from >0.25° on the volcano flank side to <0.15° on the lowlands side. The roughness increases again to the north, forming a crescent-shape region smoother than its surroundings, perhaps related to a volcanic episode.

Another area of particular geological interest in Sinus Meridiani. Recently, probable hematite mineralization has been identified there [*Christensen et al.*, 2000] by the Thermal Emission Spectrometer (TES), an instrument also on board MGS. In Plate 3 topography and median slope maps for this region are shown, as well as the mapped distribution of hematite from *Christensen et al.* [2001]. The presence of hematite closely correlates with a smoother region of median slopes <0.4°. However, the region appears to have a southwesterly slope and is not a closed depression. *Christensen et al.* [2000] examined two classes of hematite formation mechanisms: one that requires significant amounts of near surface water, and one that does not. The unusual

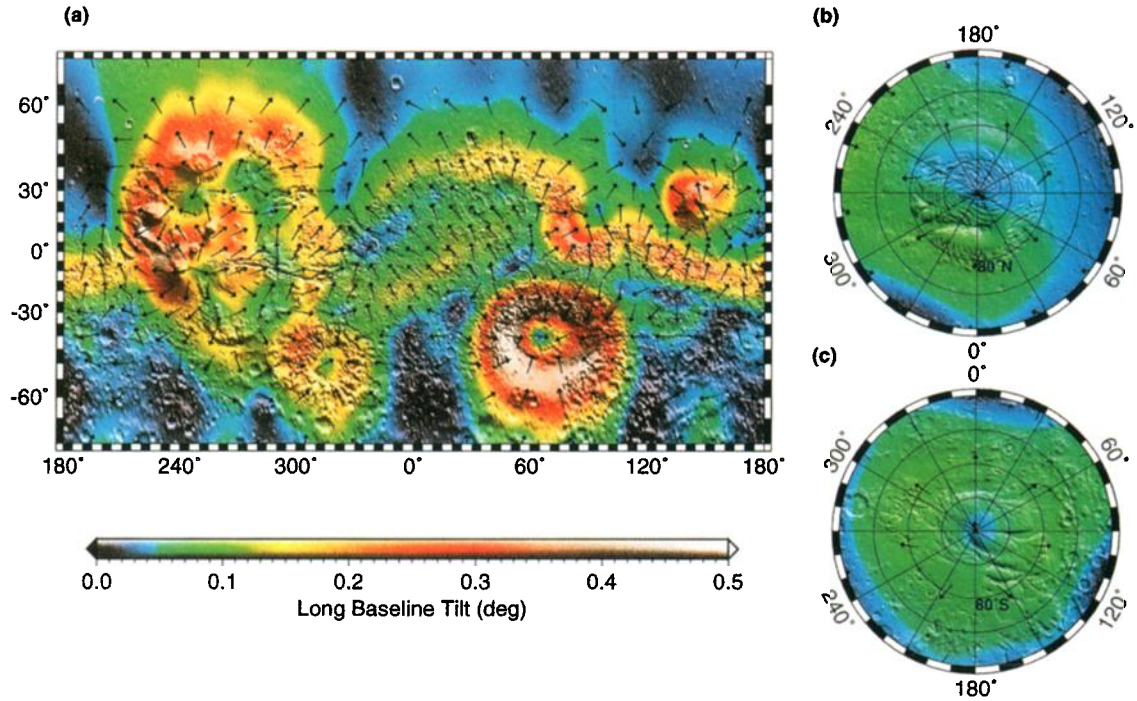

Plate 1. Long-baseline (1000 km) tilts. Azimuths are indicated by arrows, and magnitude by color. The fields are in (a) Mercator and (b and c) stereographic projections over the poles. A northeasterly illuminated shaded relief model of the topography is superimposed in monochrome. Note the northerly tilt of much of the northern hemisphere.

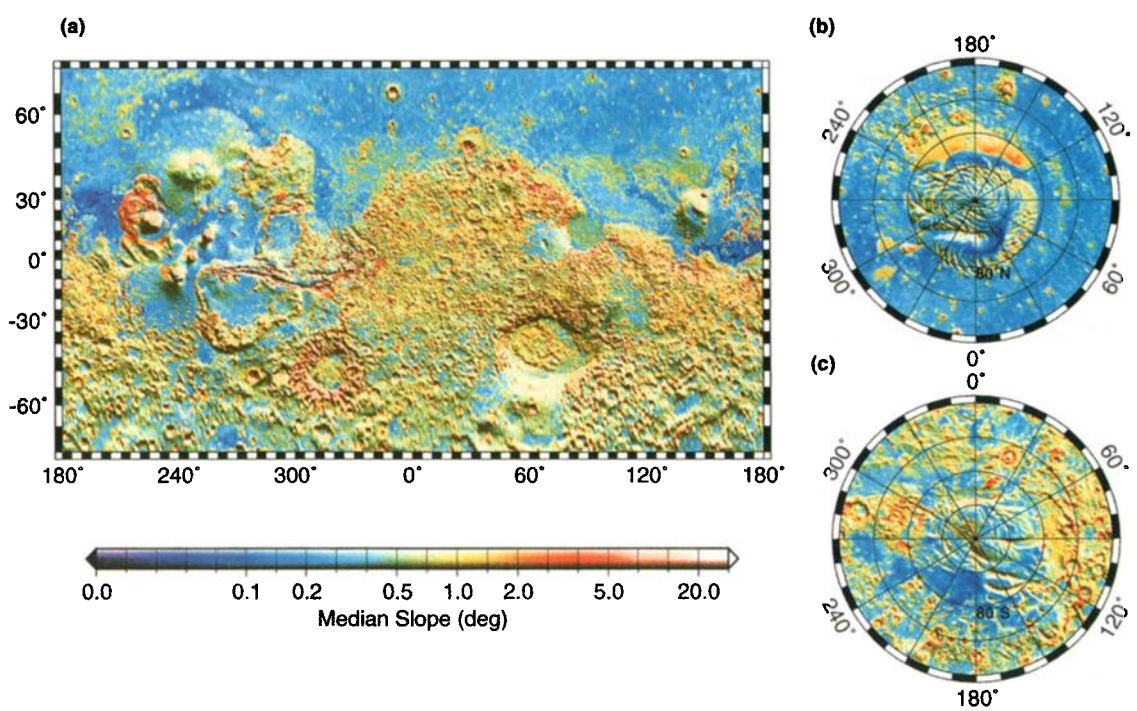

Plate 2. Median slopes in 35-km windows. Format is the same as in Plate 1. The color scale is nonlinear in order to maintain much of the dynamic range. The tick marks are spaced linearly between labels.

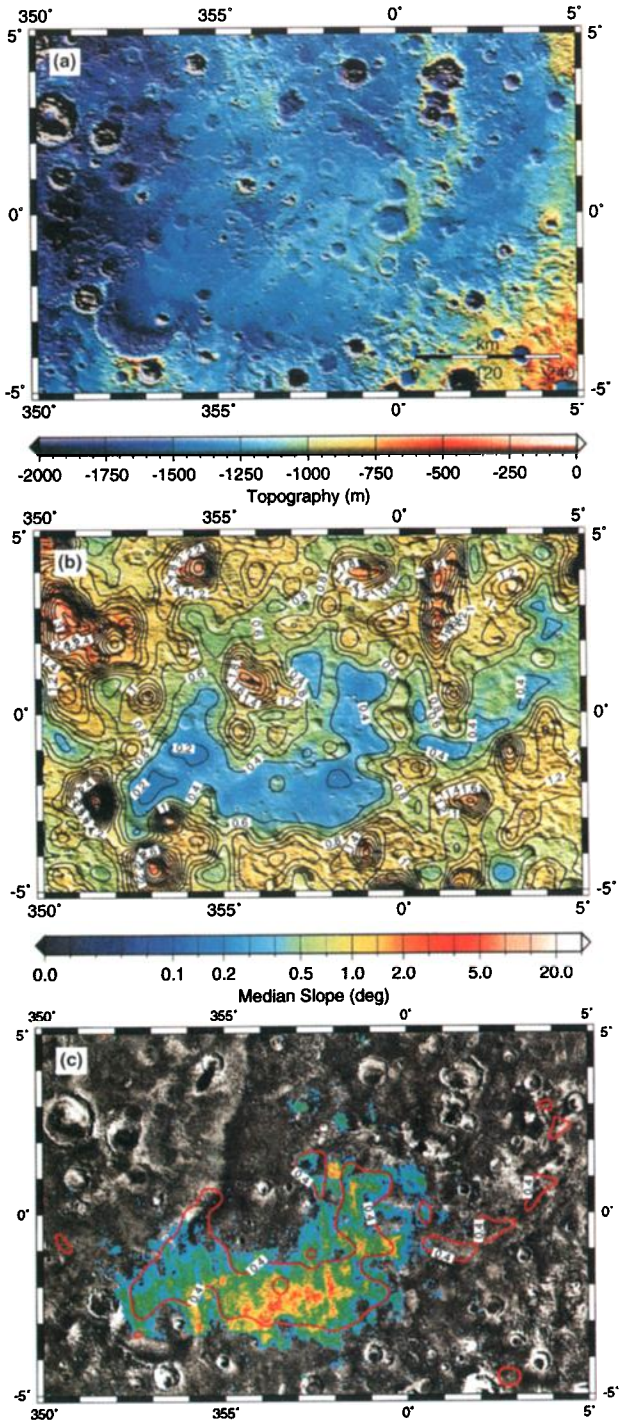

Plate 3. The Sinus Meridiani region. Shown are (a) topography, (b) median slopes, and (c) Hematite distribution from *Christensen et al.* [2001] plotted over an image mosaic of the region, with the 0.4° median absolute slope contour also indicated.

smoothness, if a result of subaqueous sedimentation, favors the first explanation over the latter.

In summary, the measured median slopes are bounded at the lowest values by Amazonis Planitia and some polar cap deposits (further discussion of this will follow). At the highest variation of slope, in order of increasing median, are the Hellas rim, Argyre rim, dichotomy boundary (especially east of 30°E), Olympus Mons aureole, and canyon walls of Valles Marineris, which are in excess of 20°.

6. Interquartile Scale

It is often useful to consider roughness in terms of typical relative elevation deviations rather than slope. One way to achieve this to employ the interquartile scale (IQS). In this characterization we measure the width of a histogram of the 50% most significant elevations, scaled to unity for a normal distribution. Before normalization, this estimator R_q is defined [*Neumann and Forsyth*, 1995] as

$$R_q = \frac{N}{2N-1}(Q_3 - Q_1), \tag{2}$$

where Q_i is the elevation of the ith quartile point and N is the number of points. To normalize, R_q is divided by 0.673, the IQS of a normal distribution. The parameter R_q is a robust estimator in the sense that it is not sensitive to outliers in as much as half of the population. This calculation is applied to all range returns that fall within a window sliding along each profile. Although choice of window size can affect the numerical values measured, the qualitative results below remain true (as is the case for the other estimators presented). In its rank 1 statistical nature, IQS is comparable to median slope except that it operates directly on elevations rather than elevation difference (slope). To avoid a regional slope bias, a mean trending surface is removed prior to the calculation. The results, computed in 35-km windows, are plotted in Plate 4. One advantage of IQS measurements is that they can be directly compared to vertical roughness as determined from MOLA pulse width measurements [*Garvin and Frawley*, 2000]. The pulse width is sensitive to roughness on smaller scales, up to the laser spot size of ~100 m on the ground. Comparison with the vertical roughness reported by *Smith et al.* [this issue] shows good relative agreement, with the absolute values systematically greater for the larger-scale IQS.

Some observational examples of the IQS measurements over various geological provinces are presented below. Many qualitative observations also appear in the median slopes characterizations.

The northern hemisphere is flat, with a typical interquartile scale of a few tens of meters ranging over thousands of kilometers [*Aharonson et al.*, 1998]. The Olympus Mons aureole deposits are among the roughest surfaces observed, with a typical IQS of hundreds of meters. Compared with the surrounding terrain and the rest of the southern hemisphere, where typical IQS is >30 m, the southwest portion of the Hellas impact basin rim appears smoother, with an IQS decreasing to ~10-30 m and extending essentially to the pole. This smoothness has been suggested to be a result of interaction with surface ice [*Kargel and Strom*, 1992], perhaps related to the nearby south polar cap.

The most unusual region is Amazonis Planitia, an area to the northwest of Olympus Mons of Amazonian age and elevation of approximately -4.1 km. This surface displays

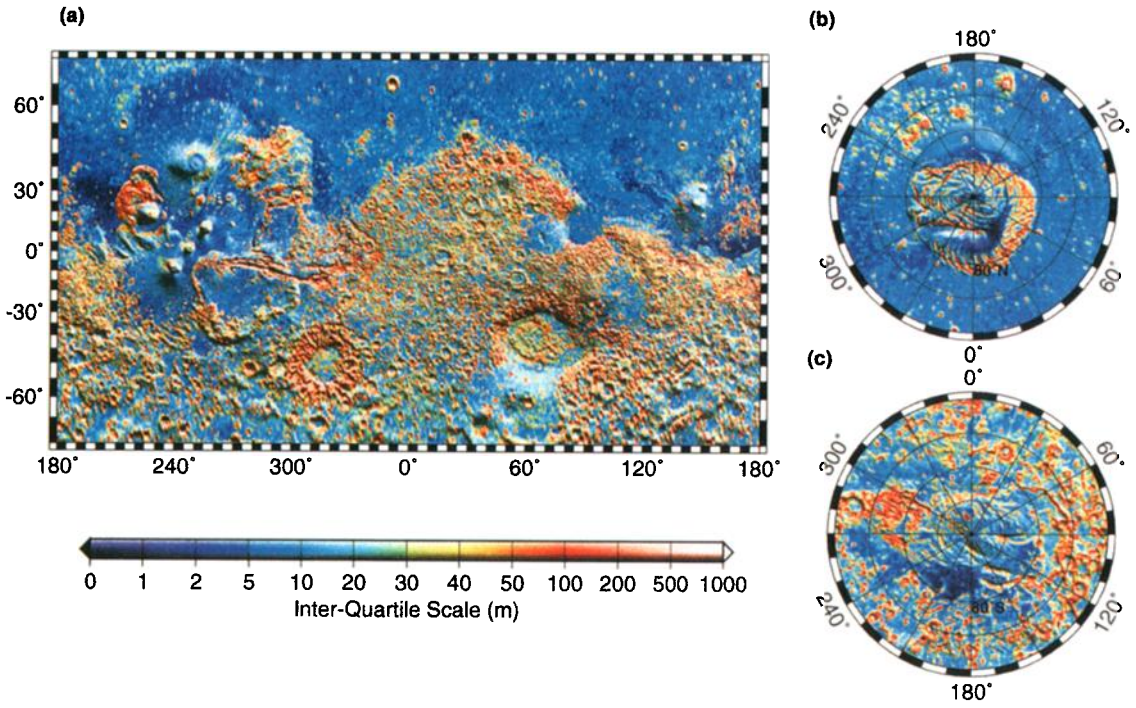

Plate 4. Interquartile scale (IQS) in 35-km windows. Format is the same as in Plate 1. Note the smoothness of Amazonis Planitia (16°N, 201°E).

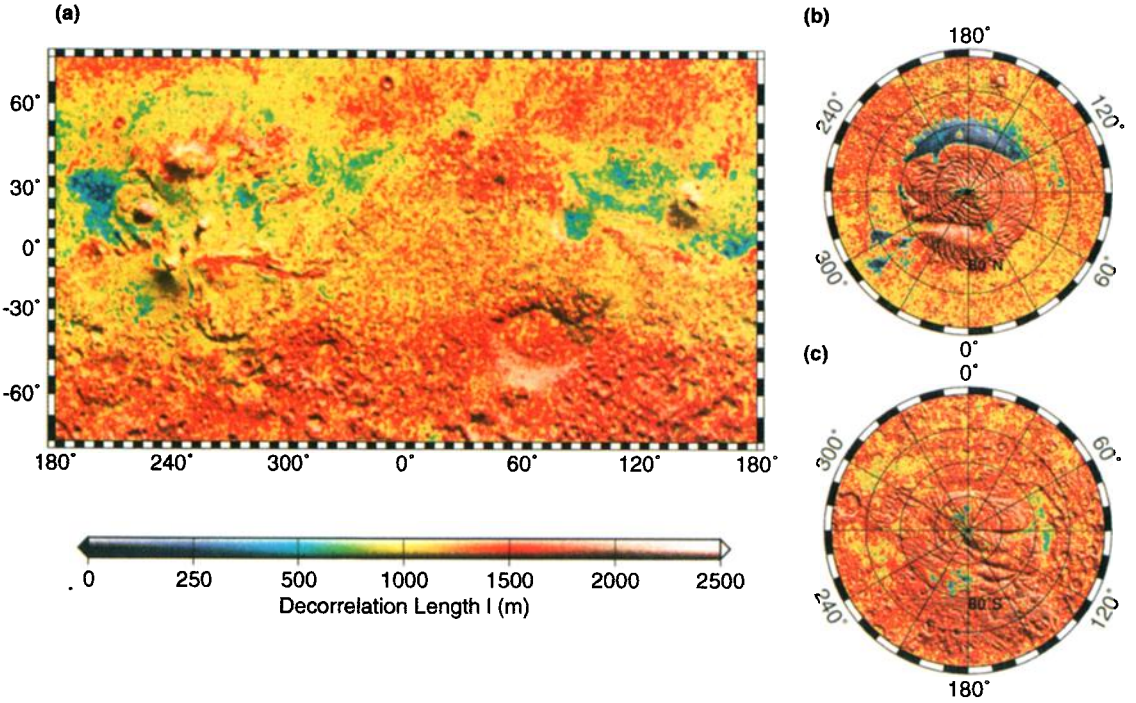

Plate 5. Decorrelation length l in 35-km windows. Format is the same as in Plate 1. Olympia Planitia (82°N, 166°E) dune fields have distinctly low decorrelation length. A latitudinal trend shifted slightly northward is seen, with typical values increasing poleward by ~50%.

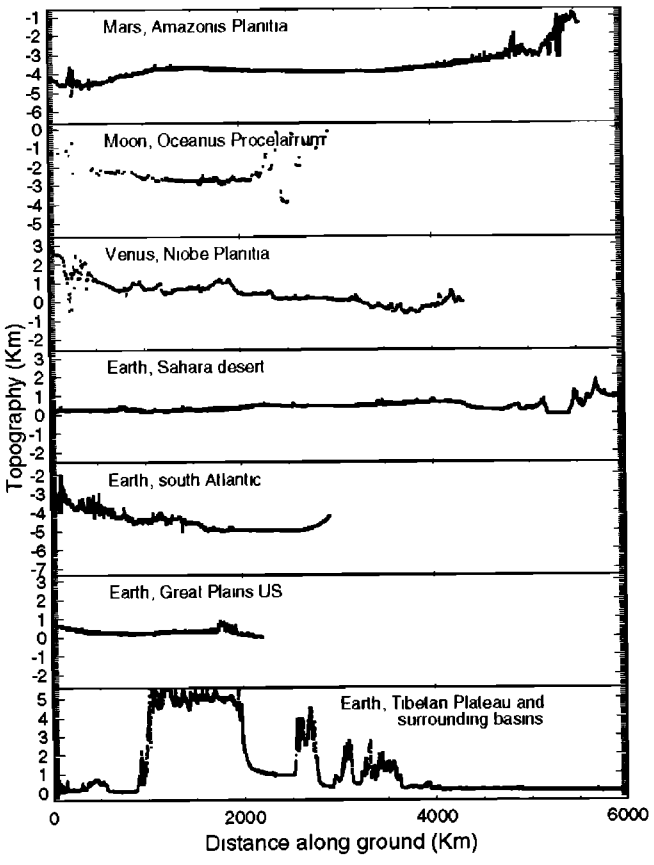

Figure 4. Comparison of planetary surface topography [from *Aharonson et al.*, 1998]. The data sets used are listed in Table 1.

an IQS variation in topography of only a few meters (still greater than the instrument's range resolution), extending over hundreds of kilometers and correlating well with the previously mapped geology. The smoothest part of the surface corresponds to member 3 of the Arcadia Formation, which was previously interpreted to consist largely of lava flows and small volcanos [*Scott and Tanaka*, 1986; *McEwen et al.*, 1999]. Member 3 also forms smooth plains west of the Olympus Mons aureoles and displays occasional flow fronts in Viking images. This area has an anomalously low thermal inertia (between 2 and 3 $\times 10^{-3}$ cal cm^{-2} s$^{-1/2}$ K^{-1} [*Christensen and Moore*, 1992]) with very low variability over tens of kilometers scale and anomalously low radar backscatter crosssection at a variety of wavelengths [*Jakosky and Muhleman*, 1981]. It has more recently been interpreted to be accumulations of fine-grained dust [*Christensen*, 1986]. The low surface roughness detected by MOLA is consistent with this interpretation but does not uniquely explain the genesis of this region.

An initial step toward identifying the mechanism of formation of Amazonis Planitia is to compare its topographic properties to other smooth regions with potentially analogous origins. Shown in Figure 4 are profiles of elevation collected by various altimeters over smooth surfaces from a variety of solar system bodies. The data sets used are listed in Table 1. At the top is MOLA pass 31 over Amazonis Planitia, where the anomalously smooth region is observed to extend over 600 km, approximately centered in the plot. Below is a Clementine profile of the Moon's Oceanus Procellarum, Magellan radar altimetry over one of the smoothest areas of Venus, Niobe Planitia, Shuttle Laser Altimeter data collected over the Sahara desert, and shiptracks of Seabeam 2200 bathymetry over the South Atlantic abyssal plains. The last two profiles were extracted from the GTOPO data set, first over the Great Plains in the United States and second over the Indo-Gangedic Plains across over the Tibetan Plateau, down across the Tarim Basin, and continuing northward. Oceanus Procellarum consists of lava flows that have been broadly tilted by subsidence and locally steepened by tectonic deformation (wrinkle ridges); their small-scale roughness is dominated by impact regolith formation processes. Niobe Planitia on Venus consists of vast lava plains similarly tilted and steepened but not influenced by regolith formation [*Tyler et al.*, 1992]. Comparison of these surfaces reveals that of these lowest, smoothest regions observed in the solar system, Amazonis Planitia closely resembles in its smoothness only the heavily sedimented surfaces on the Earth, i.e., oceanic abyssal plains and basins filled by fluvial deposition processes. It is noteworthy that volcanically resurfaced terrain is markedly rougher on the Moon, on Venus, and on Mars than the peculiar Amazonis deposits. Saharan sand sheets are rougher in terms of IQS by a factor of ~3. Other regions in the Martian northern hemisphere that exhibit evidence of dust deposition are rougher than Amazonis as well.

Table 1. Data Sets Used in the Planetary Surface Comparison of Figure 4 and Their Approximate Horizontal Resolution and Vertical Accuracy.

Planet	Instrument / Source	Region	Accuracy, m	Resolution, km	Data Reference
Mars	MOLA	Amazonis Planitia	0.4	0.3	*Smith et al.* [this issue]
Moon	Clementine	Oceanus Procellarum	40	0.2[a]	*Smith et al.* [1997]
Venus	Magellan	Niobe Planitia	4	10	*Ford and Pettengill* [1992]
Earth	SLA	Sahara desert	1.5	0.7	*Garvin et al.* [1997]
Earth	Seabeam 2200	South Atlantic	2	0.1	*Neumann et al.* [1996]
Earth	GTOPO DEM	Great Plains, US	20[b]	0.1	*Gesch and Larson* [1996]
Earth	GTOPO DEM	Tibetan Plateau and basins	20[b]	0.1	*Gesch and Larson* [1996]

[a]Resolution is ~1.6 km for 1-Hz data and ~0.2 km for 8-Hz data.
[b]Highly variable.

Areas similar in size and IQS are found on Mars only at the north and south ice-covered caps.

7. Horizontal Decorrelation Length

Thus far, the vertical component of the topography has been characterized by various statistical estimators. One way to define a characteristic horizontal length scale is by estimating the distance over which the topography first decorrelates with itself. This distance is obtained by computing the autocovariance function Γ of a sample population $Y = \{y_1, \ldots, y_N\}$ as a function of the lag L and measuring its width at half maximum. The autocovariance function is estimated by

$$\Gamma(L\Delta) = \frac{1}{N}\sum_{k=1}^{N-L}(y_k - \bar{y})(y_{k+L} - \bar{y}), \quad (3)$$

where Δ is the sampling interval, N is the number of samples in the window, and $\bar{y}$ is the mean of Y. The length l, given by

$$\Gamma(l) = \frac{1}{2}\Gamma(0), \quad (4)$$

measures the width of the central peak in the autocovariance function. Hence, in the ensuing discussion, l as defined in (4) will be referred to as a decorrelation length. Other definitions are possible. The conventional definition for the correlation length can be used to estimate l' with

$$l' = \sqrt{\frac{\sum_{k=1}^{N} x_k^2\,\Gamma(x_k)}{\sum_{k=1}^{N}\Gamma(x_k)}}. \quad (5)$$

Here we measure l, rather than l', because l does not depend on the behavior of Γ at large lags. The value of l still depends on window size, but its relative variations over the Martian surface do not. In the following analysis, 35-km windows were employed, as before.

Plate 5 shows a map view of the decorrelation length. Several interesting trends emerge. First, a global equator-to-pole increase in decorrelation length is visible from ~1000 m at the equator to ~1800 m near both poles. *Kreslavsky and Head* [2000] observed a similar latitudinal trend in their roughness estimator and suggest that it is related to seasonal deposition/sublimation cycles or alternatively to terrain-softening effects (also seen in changes in crater morphology by *Garvin et al.* [2000]). In the northern hemisphere there is an additional drop in l to ~500 m at several locations (Utopia Planitia, Isidis, northern Chryse Planitia) and a unique drop to ~250 m at Amazonis Planitia. By interpolating the autocovariance function, even shorter values for l are observed distinctly at the polar dune fields, especially in Olympia Planitia (82°N, 166°E). Values of l that are smaller than the sampling distance (~300 m) should be regarded with caution, because they rely on an extrapolation beyond the shortest wavelength observed.

8. Power Spectral Analysis

One of the most intriguing hypotheses that has arisen on the basis of data from MGS is the possibility of an ancient liquid water ocean residing in the northern lowlands [*Head et al.*, 1998, 1999]. The relative smoothness of the lowlands, it has been suggested, resulted from sedimentation processes that are expected on an ocean floor. In this section one test of this hypothesis is considered.

Two areally large regions on Mars have been selected to represent the heavily cratered terrain in the south (region A) and the smooth terrain in the north (region B). Region A is bounded by latitudes 60°S and 30°S and by longitudes 150°E and 210°E. This is the most ancient, heavily cratered crust on Mars, where strong magnetic anomalies have been observed. Region B surrounds the planet in longitude and is bounded by latitudes 60°N-75°N.

The large number of MOLA profiles allows a highly accurate estimation of the power spectrum. In Figure 5 the means of one-dimensional spectra along MOLA profiles in these regions are plotted. If the spectrum is roughly divided in two, a short-wavelength portion ($0.7<\lambda<7$ km) and a long-wavelength portion ($20<\lambda<200$ km), then it is seen that although the magnitude of the power in short wavelengths is smaller in region B than in region A, the slope is almost unchanged. However, the slope of the long-wavelength portion is substantially reduced in region B relative to A.

There is a large body of work on descriptions of scaling relationships in terms of geomorphological models (reviewed by *Dodds and Rothman* [2000]). One simple model for the complex process of sedimentation consists of a diffusion process forced with random noise [*Edwards and Wilkinson*, 1982]. Figure 6 illustrates a surface evolving under these conditions. The cartoon shows falling particles being deposited on the surface giving rise to the noise term, with downslope movement of material giving rise to the diffusive term. With this model it is possible to consider if the spec-

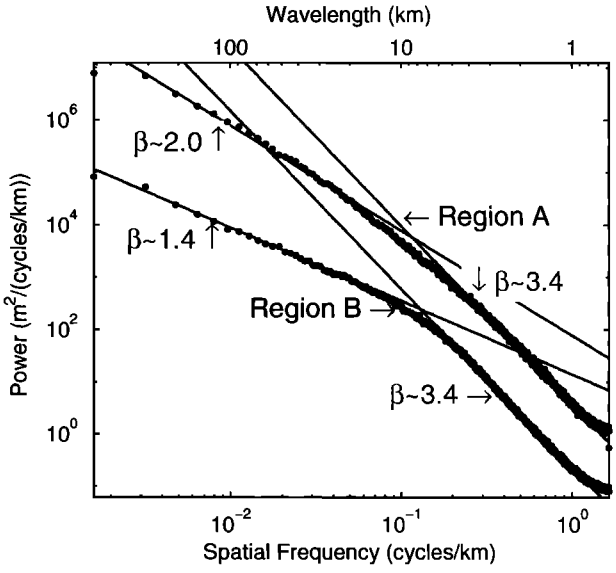

Figure 5. Average power spectrum of the topography of an area in the heavily cratered southern terrain (region A) and of an area in the northern lowlands (region B). Note the logarithmic scale, so that slopes indicate power law exponents. In the short wavelengths the effective exponents for the two regions are similar, while in the long wavelengths the exponent of region B is lower than that of region A.

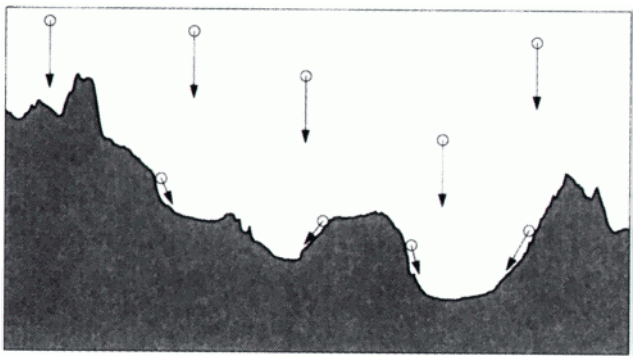

Figure 6. Cartoon showing the growth of a surface under a model of noisy diffusion.

tral content of the lowlands appears simply as a diffusively smoothed version of an initially heavily cratered southern terrain. Regardless of the details, it is expected that any reasonable model would predict that short wavelengths evolve fastest and long wavelengths equilibrate last. For the case of a diffusive model, simple dimensional analysis with a diffusion constant ν, the timescale τ_k for decay of modes of wave number k will be inversely proportional to νk^2. In the steady state limit the spectrum should decay as k^{-2} [*Nattermann and Tang*, 1992; *Edwards and Wilkinson*, 1982].

In a frame comoving with the average height of the surface, the continuum limit of the above model is described by the Edwards-Wilkinson equation [*Edwards and Wilkinson*, 1982], solved in Appendix A with the explicit inclusion of initial conditions. The evolution in time of an average initial spectrum $S(\mathbf{k}, 0)$, given by equation (A11), is

$$S(\mathbf{k}, t) = e^{-2\nu k^2 t} S(\mathbf{k}, 0) + \frac{(2\pi)^2 \eta_0^2}{2\nu k^2} \left(1 - e^{-2\nu k^2 t}\right), \quad (6)$$

where the term on the left-hand side is the time-dependent power spectrum, ν is the diffusion constant, η_0 is the amplitude of the noise, k is magnitude of the 2-D wave vector $\mathbf{k}$, and t is time. Note that as intuition suggested, noisy diffusion affects short-wavelength features (large k in the exponential term) first and that long-wavelength features (small k) are affected last. Furthermore, in the steady state limit the power law exponent predicted in two dimensions is $\beta_r = 2$ (where $S(k) \propto k^{-\beta_r}$). One-dimensional transects taken from this 2-D field will theoretically have an exponent $\beta = 1$ [*Voss*, 1991; *Neumann and Forsyth*, 1995], but in practice the exponent can be greater ($\sim$1.2) owing to finite domain size effects.

The power law exponent in the spectral range of wavelengths 20-200 km shown in Figure 5 region B is consistent with evolution of the surface by the above model of sedimentation. In the decade of wavelengths from 0.7 to 7 km the data cannot be explained by noisy diffusion alone, nor in fact by most reasonable models, because they predict fast short-wavelength mode relaxation and slow relaxation in the long wavelengths. A satisfactory explanation of the spectral evolution requires an additional process to steepen the slope of the short wavelengths. Such a process could, for example, be cratering. With an appropriate size frequency distribution it can account for the observed power law exponent $\beta \sim 3.4$ for the high-frequency content of both regions. Since large impactors, and therefore large cratering events, are rare, the shallowing of the long-wavelength portion of the spectrum from a slope of $\sim$2.1 to $\sim$1.4 can be accounted for by a smoothing, diffusion-like process that acts on a faster timescale than the large craters (though still slower than the short-wavelength diffusion).

We therefore conclude that under the assumption of a noisy diffusion model for sedimentation, the lowlands appear as a partially smoothed version of the south in a limited wavelength range. The spectral character can be explained by a diffusive process at long wavelengths, followed by, or concurrent with, cratering at short wavelengths. The possibility that the spectrum of the lowlands was smoothed completely (effectively resetting the surface topography) and then evolved further to its present shape is not excluded by this analysis.

9. Landing Site Selection

Of primary importance for the selection of sites for upcoming Mars landers is the threat posed to the safety of the spacecraft on touchdown, the vehicle's likely tilt, and possibly the maneuverability at the site. Such considerations

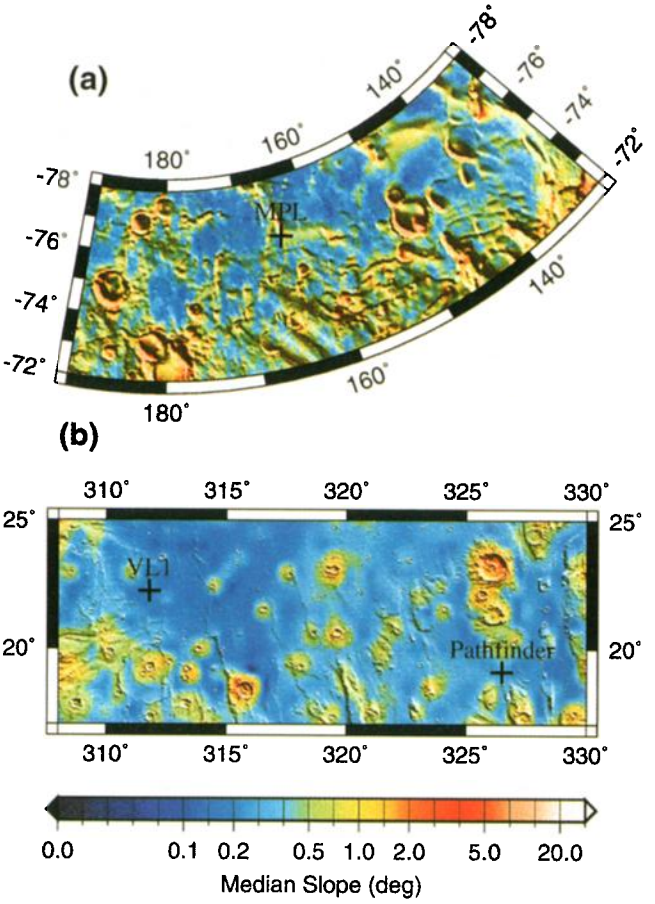

Plate 6. Median slope roughness maps of (a) area accessible to the Mars Polar Lander and (b) Viking Lander 1 and Pathfinder sites in Chryse Planitia.

were employed, for example, in the site selection for Viking Lander 2 using radar cross-section data. Although the topographic wavelengths most relevant are smaller than the resolution of MOLA data, the dependence of vertical roughness on scale is typically monotonic. Therefore MOLA data are a powerful discriminator among surfaces in a comparative sense, which can be further calibrated with ground truth.

In Plate 6 we demonstrate the use of MOLA to help characterize past landing sites. Plate 6a shows median slope roughness for the area that was accessible to the Mars Polar Lander (MPL). The expected current position of the spacecraft is also indicated. At MOLA sampling, smooth plains are prevalent in an area south of 75°S between longitudes 140°E and 180°E, but higher slopes are observed in localized inliers. As shown in Plate 6b median slopes of the smooth plains in Chryse Planitia have typical values between 0.15° and 0.3° (as expected, lower than the RMS slope values). The relative smoothness at this scale is consistent with the surface being a depositional in origin. Viking Lander 1 and Pathfinder landed in this area and provide ground truth for radar [*Harmon*, 1997] and MOLA-derived roughness at small scales. The Pathfinder landing site, situated at the mouth of Ares Vallis, is characterized by deposited debris of channelized flows. *Golombek et al.* [1996] find measured slopes there are consistent with an RMS of ~5°.

10. Conclusions

The results discussed here represent a snapshot of an ongoing data analysis effort which is progressing in terms of both data volume and coverage, as well as in theory and technique. Thus far, we have demonstrated the advantages of robust estimators over traditional ones and have used them to characterize the Martian surface globally. The global asymmetry in the crust of Mars manifests itself in the bimodality of the hypsometry, but the elevation distribution function becomes unimodal when referenced to the planetary COF, similar to Venus but not Earth. Outflow channels often follow the direction of long-baseline slopes in the topography. These tilts are mostly facing north in the northern hemisphere and in some parts of the south. It was found that at MOLA sampling baselines the northern hemisphere is smoother than the south and that the vast region of Amazonis Planitia is unusually smooth. Of the measured terrestrial planets' topography, Amazonis is most analogous to heavily sedimented fluvial basins on Earth such as the ocean floor. Although this observation represents a piece of circumstantial evidence rather than proof of geologic origin, and despite its very early emergence from MOLA data, it has potentially tantalizing ramifications and has so far withstood the tests of repeated measurements and global coverage.

Statistics of topography show that a part of Hellas's rim has undergone intensified erosion, consistent with a hypothesis of smoothing by an ancient glacier or much larger south polar cap. We have further shown how the decorrelation length can be used as a discriminator among geologic surfaces and measured a very short correlation length over the dunes of Olympia Planitia.

A description of the topography in terms of its power spectrum demonstrates the difference between the lowlands and highlands. Modification of the long-wavelength portions of the north's spectrum relative to the south's can be accounted for by a simple depositional model (i.e. noisy diffusion) such as might be expected at an ocean's floor. However, the short-wavelength spectrum cannot by simultaneously matched, and its explanation requires an additional process such as cratering.

MOLA slopes and statistical properties of topography are also being used to characterize potential landing sites for future Mars landers.

Appendix A: Power Spectrum Evolution Under Noisy Diffusion With Initial Conditions

The effect of many physical processes on the height of a two-dimensional interface $h(\mathbf{x}, t)$ as a function of position and time can be modeled with the noisy diffusion equation, which can be derived from the continuum limit of a lattice model of sedimentation [*Edwards and Wilkinson*, 1982]:

$$\frac{\partial}{\partial t} h(\mathbf{x}, t) = \nu \nabla^2 h(\mathbf{x}, t) + \eta(\mathbf{x}, t), \tag{A1}$$

where ν is a diffusion constant and $\eta(\mathbf{x}, t)$ is a noisy forcing term that is uncorrelated in the ensemble average:

$$\langle \eta(\mathbf{x}', t')\, \eta(\mathbf{x}, t) \rangle = \eta_0^2\, \delta^2(\mathbf{x} - \mathbf{x}')\, \delta(t - t'). \tag{A2}$$

As have others in the past [e.g., *Edwards and Wilkinson*, 1982; *Barabási and Stanley*, 1995; *Nattermann and Tang*, 1992], we seek a spectral domain time-dependent solution to equation (A1). Here we explicitly include a prescribed initial condition so that we may examine the evolution of one surface from another (B. Newman, personal communication, 2000).

Rearranging the Edwards-Wilkinson equation (A1), and correlating it with itself gives

$$\left(\frac{\partial}{\partial t} - \nu \nabla^2\right)\left(\frac{\partial}{\partial t'} - \nu \nabla'^2\right) \langle h(\mathbf{x}, t) h(\mathbf{x}', t') \rangle = \langle \eta(\mathbf{x}', t')\, \eta(\mathbf{x}, t) \rangle . \tag{A3}$$

Assuming that the field h is stationary in space, the correlation function ρ depends only on $\mathbf{x} - \mathbf{x}'$, and we define

$$\rho(\mathbf{x} - \mathbf{x}', t, t') = \langle h(\mathbf{x}, t) h(\mathbf{x}', t') \rangle . \tag{A4}$$

Furthermore, $\nabla^2 \rho = \nabla'^2 \rho$, we can replace $\mathbf{x} - \mathbf{x}'$ with $\mathbf{x}$ and substitute (A2) and (A4) into (A3), to obtain

$$\left(\frac{\partial}{\partial t} - \nu \nabla^2\right)\left(\frac{\partial}{\partial t'} - \nu \nabla^2\right) \rho(\mathbf{x}, t, t') = \eta_0^2\, \delta^2(\mathbf{x})\, \delta(t - t'). \tag{A5}$$

Multiplication by $e^{-i\mathbf{k}\cdot\mathbf{x}}$, and integration over all $\mathbf{x}$, yields

$$\left(\frac{\partial}{\partial t} - \nu k^2\right)\left(\frac{\partial}{\partial t'} - \nu k^2\right) S(\mathbf{k}, t, t') = (2\pi)^2 \eta_0^2 \delta(t - t'), \tag{A6}$$

where $k = |\mathbf{k}|$, and S is defined as

$$S(\mathbf{k}, t, t') = \frac{1}{(2\pi)^2} \int \rho(\mathbf{x}, t, t') e^{-i\mathbf{k}\cdot\mathbf{x}} d\mathbf{x}, \qquad \text{(A7)}$$

assuming that ρ decays with $|\mathbf{x}| \to \infty$ sufficiently fast that the integral converges, i.e., that the Fourier transform of the correlation function exists. When $t = t'$, we identify $S(\mathbf{k}, t, t) \equiv S(\mathbf{k}, t)$ as the power spectrum, in accordance with the Wiener-Khinchine theorem [e.g., *Gardiner*, 1985].

Rearrangement (using an integrating factor) of the left-hand side of (A6) yields

$$e^{\nu k^2 (t+t')} \frac{\partial}{\partial t'} \frac{\partial}{\partial t} e^{\nu k^2 (t+t')} S(\mathbf{k}, t, t') = (2\pi)^2 \eta_0^2 \delta(t - t'). \qquad \text{(A8)}$$

Multiplying by $e^{-\nu k^2 (t+t')}$, integrating from 0 to t and 0 to t', and finally taking the particular case $t = t'$ gives, after some algebra (allowing for both $t < t'$ and $t > t'$),

$$S(\mathbf{k}, t) = e^{-\nu k^2 t} S(\mathbf{k}, t, 0) + e^{-\nu k^2 t} S(\mathbf{k}, 0, t) - e^{-2\nu k^2 t} S(\mathbf{k}, 0, 0) + \frac{(2\pi)^2 \eta_0^2}{2\nu k^2} \left(1 - e^{-2\nu k^2 t}\right). \qquad \text{(A9)}$$

By assuming that the initial field and the stochastic forcing are uncorrelated, so that, for example, $\langle \eta(\mathbf{x}, t) h(\mathbf{x}', 0) \rangle = 0$, we can multiply (A1) by $h(\mathbf{x}', 0)$ and repeat the above steps to find

$$S(\mathbf{k}, t, 0) = S(\mathbf{k}, 0, t) = e^{-\nu k^2 t} S(\mathbf{k}, 0, 0). \qquad \text{(A10)}$$

Taking $S(\mathbf{k}, 0) \equiv S(\mathbf{k}, 0, 0)$ as the spectrum of the initial field, and substituting (A10) into (A9), the time-dependent power spectrum is

$$S(\mathbf{k}, t) = e^{-2\nu k^2 t} S(\mathbf{k}, 0) + \frac{(2\pi)^2 \eta_0^2}{2\nu k^2} \left(1 - e^{-2\nu k^2 t}\right). \qquad \text{(A11)}$$

Acknowledgments. We thank John Goff and Bill Newman for careful reviews and acknowledge helpful discussions with Greg Neumann and Jim Head. It was our pleasure to incorporate comments by Bill Newman on an early draft of this paper, which helped formulate Appendix A in a more precise manner. This study was supported by the generous Kerr Fellowship, the Mars Global Surveyor Project, and by DOE grant DE FG02-99ER 15004.

References

Aharonson, O., M. T. Zuber, G. A. Neumann, D. E. Smith, and J. W. Head, Mars: Northern hemisphere slopes and slope distributions, *Geophys. Res. Lett.*, *25*, 4413–4416, 1998.

Aharonson, O., M. T. Zuber, G. A. Neumann, D. E. Smith, and J. W. Head, Second order statistics of topography of the northern hemisphere of Mars from MOLA, *Lunar and Planet. Sci.*, *XXX*, abstract 1792, 1999.

Albee, A. L., F. D. Palluconi, and R. E. Arvidson, Mars Global Surveyor mission: Overview and status, *Science*, *279*, 1671–1672, 1998.

Albee, A. L., F. D. Palluconi, and R. E. Arvidson, Overview of the Mars Global Surveyor mission, *J. Geophys. Res.*, this issue.

Banerdt, W. B., and A. Vidal, Surface drainage on Mars, *Lunar Planet. Sci.*, *XXXII*, abstract 1488, 2001.

Barabási, A.-L., and H. E. Stanley, *Fractal Concepts in Surface Growth*, Cambridge Univ. Press, New York, 1995.

Carr, M. H., *The Surface of Mars*, Yale Univ. Press, New Haven, Conn., 1981.

Christensen, P. R., Regional dust deposits on Mars: Physical properties, age, and history, *J. Geophys. Res.*, *91*, 3533–3545, 1986.

Christensen, P. R., and H. J. Moore, The Martian surface layer, in *Mars*, edited by H. H. Kieffer et al., pp. 686–729, Univ. of Ariz. Press, Tucson, 1992.

Christensen, P. R., et al., Detection of crystalline hematite mineralization on Mars by the Thermal Emission Spectrometer: Evidence for near-surface water, *J. Geophys. Res.*, *105*, 9623–9642, 2000.

Christensen, P. R., R. V. Morris, M. D. Lane, J. L. Bandfield, and M. C. Malin, Global mapping of Martian hematite mineral deposits: Remnants of water-driven processes on early Mars, *J. Geophys. Res.*, *in press*, 2001.

Dodds, P. S., and D. H. Rothman, Scaling, universality, and geomorphology, *Annu. Rev. Earth Planet. Sci.*, *28*, 571–610, 2000.

Edwards, S. F., and D. R. Wilkinson, The surface statistics of a granular aggregate, *Proc. R. Soc. London, Ser. A*, *381*, 17–31, 1982.

Esposito, P. B., W. B. Banerdt, G. F. Lindal, W. L. Sjogren, M. A. Slade, B. G. Bills, D. E. Smith, and G. Balmino, Gravity and topography, in *Mars*, edited by H. H. Kieffer et al., pp. 209–248, Univ. of Ariz. Press, Tucson, 1992.

Ford, P. G., and G. H. Pettengill, Venus topography and kilometer-scale slopes, *J. Geophys. Res.*, *97*, 13,103–13,114, 1992.

Fox, C. G., and D. E. Hayes, Quantitative methods for analyzing the roughness of the seafloor, *Rev. Geophys.*, *23*, 1–48, 1985.

Gardiner, C. W., *Handbook of Stochastic Methods for Physics, Chemistry and the Natural Sciences*, 2nd ed., Springer-Verlag, New York, 1985.

Garvin, J. B., J. L. Bufton, J. B. Blair, S. B. Luthcke, J. J. Frawley, and J. A. Marshall, Observations of the Earth's topography from the Shuttle Laser Altimeter (SLA): Laser pulse echo recovery measurements of terrestrial surfaces, paper presented at *European Geophysical Society Meeting*, Vienna, 1997.

Garvin, J. B., and J. J. Frawley, Global vertical roughness of Mars from Mars Orbiter Laser Altimeter pulse-width measurements, *Lunar Planet. Sci.*, *XXXI*, abstract 1884, 2000.

Garvin, J. B., S. E. Sakimoto, J. J. Frawley, and C. Schnetzler, Geometric properties of Martian impact craters: An assessment from the Mars Orbiter Laser Altimeter (MOLA) digital elevation modes, *Lunar Planet. Sci.*, *XXXI*, abstract 1619, 2000.

Gesch, D. B., and K. S. Larson, Techniques for development of global 1-kilometer digital elevation models, paper presented at *Pecora Thirteen: Human Interactions With the Environment - Perspectives From Space*, Sioux Falls, S.D., Aug. 20-22, 1996.

Goff, J. A., and T. H. Jordan, Stochastic modeling of seafloor morphology: Inversion of sea beam data for second-order statistics, *J. Geophys. Res.*, *93*, 13,589–13,608, 1988.

Golombek, M. P., et al., Overview of the Mars Pathfinder mission and assessment of landing site predictions, *Science*, *278*, 1743–1748, 1996.

Harmon, J. K., A radar study of the Chryse region, Mars, *J. Geophys. Res.*, *102*, 4081–4095, 1997.

Harmon, J. K., R. E. Arvidson, E. A. Guinness, B. A. Campbell, and M. A. Slade, Mars mapping with delay-Doppler radar, *J. Geophys. Res.*, *104*, 14,065–14,090, 1999.

Head, J. W., M. Kreslavsky, H. Hiesinger, M. Ivanov, S. Pratt, N. Seibert, D. E. Smith, and M. T. Zuber, Oceans in the past history of Mars: Tests for their presence using Mars Orbiter Laser Altimeter (MOLA) data, *Geophys. Res. Lett.*, *25*, 4401–4404, 1998.

Head, J. W., H. Hiesinger, M. A. Ivanov, M. A. Kreslavsky, S. Pratt, and B. J. Thomson, Possible oceans on Mars: Evidence from Mars Orbiter Laser Altimeter data, *Science*, *286*, 2134–2137, 1999.

Jakosky, B. M., and D. O. Muhleman, A comparison of the thermal and radar characteristics of Mars, *Icarus*, *45*, 25–38, 1981.

Kargel, J., and R. Strom, Ancient glaciation on Mars, *Geology*, *20*, 3–7, 1992.

Kreslavsky, M. A., and J. W. Head, Kilometer-scale slopes on Mars and their correlation with geologic units: Initial results from Mars Orbiter Laser Altimeter (MOLA) data, *J. Geophys. Res.*, *104*, 21,911–21,924, 1999.

Kreslavsky, M. A., and J. W. Head, Kilometer-scale roughness of Mars: Results from MOLA data analysis, *J. Geophys. Res.*, *105*, 26,695–26,711, 2000.

Lemoine, F. G., D. D. Rowlands, D. E. Smith, D. S. Chinn, D. E. Pavlis, S. B. Luthcke, G. A. Neumann, and M. T. Zuber, An improved solution of the gravity field of Mars (GMM-2B) from Mars Global Surveyor, *J. Geophys. Res.*, this issue.

McEwen, A. S., M. C. Malin, L. Keszthelyi, P. Lanagan, R. Beyer, and W. K. Hartmann, Recent and ancient flood lavas on Mars, *Lunar Planet. Sci.*, *XXX*, abstract 1829, 1999.

McGill, G. E., The Utopia basin revisited: Regional slope and shorelines from MOLA profiles, *Geophys. Res. Lett.*, *28*, 411–414, 2001.

Mouginis-Mark, P. J., S. H. Zisk, and G. S. Downs, Ancient and modern slopes in the Tharsis region of Mars, *Nature*, *297*, 546–550, 1982.

Mutch, T. A., R. E. Arvidson, J. W. Head, K. L. Jones, and R. S. Saunders, *The Geology of Mars*, Princeton Univ. Press, Princeton, N.J., 1976.

National Geophysical Data Center, Digital relief of the surface of the Earth, *Data Announce. 88-MGG-02*, Nat. Oceanic and Atmos. Admin., Boulder, Colo., 1988.

Nattermann, T., and L.-H. Tang, Kinetic surface roughening: I. The Kardar-Parisi-Zhang equation in the weak coupling regime, *Phys. Rev. A*, *45*, 7156–7161, 1992.

Neumann, G. A., and D. W. Forsyth, High resolution statistical estimation of seafloor morphology: Oblique and orthogonal fabric on the Mid-Atlantic ridge, *Mar. Geophys. Res.*, *17*, 221–250, 1995.

Neumann, G. A., P. J. Michael, and B. B. Hanan, Temporal variation of crustal emplacement, 33° S Mid-Atlantic ridge, *J. Conf. Abstr.*, *1*, 836–837, 1996.

Neumann, G. A., F. G. Lemoine, and D. D. Rowlands, Crossover analysis of Mars Orbiter laser altimetric data, *J. Geophys. Res.*, this issue.

Phillips, R. J., et al., Ancient geodynamics and global-scale hydrology on mars, *Science*, *291*, 2587–2591, 2001.

Rodríguez-Iturbe, I., and A. Rinaldo, *Fractal River Basins: Chance and Self-Organization*, Cambridge Univ. Press, New York, 1997.

Scheiddeger, A. E., *Theoretical Geomorphology*, 3rd ed., Springer-Verlag, New York, 1991.

Scott, D. H., and K. L. Tanaka, Geologic map of the western equatorial region of Mars, scale 1:15,000,000, *U.S. Geol. Surv. Map I-1802-A*, 1986.

Sharpton, V. L., and J. W. Head, Analysis of regional slope characteristics on Venus and Earth, *J. Geophys. Res.*, *90*, 3733–3740, 1985.

Sharpton, V. L., and J. W. Head, A comparison of the regional slope characteristics of Venus and Earth: Implications for geologic processes on Venus, *J. Geophys. Res.*, *91*, 7545–7554, 1986.

Smith, D. E., and M. T. Zuber, The shape of Mars and the topographic signature of the hemispheric dichotomy, *Science*, *271*, 184–188, 1996.

Smith, D. E., M. T. Zuber, G. A. Neumann, and F. G. Lemoine, Topography of the Moon from the Clementine lidar, *J. Geophys. Res.*, *102*, 1591–1611, 1997.

Smith, D. E., et al., The global topography of Mars and implications for surface evolution, *Science*, *284*, 1495–1503, 1999.

Smith, D. E., et al., Mars Orbiter Laser Altimeter (MOLA): Experiment summary after the first year of global mapping of Mars, *J. Geophys. Res.*, this issue.

Smith, D. K., and T. H. Jordan, Seamount statistics in the Pacific ocean, *J. Geophys. Res.*, *93*, 2899–2918, 1988.

Tanaka, K., and G. Leonard, Geology and landscape evolution of the Hellas region of Mars, *J. Geophys. Res.*, *100*, 5407–5432, 1995.

Tyler, G. L., R. A. Simpson, M. J. Maurer, and E. Holmann, Scattering properties of the Venusian surface: Preliminary results from Magellan, *J. Geophys. Res.*, *97*, 13,115–13,139, 1992.

Voss, R. F., Random fractals: Characterization and measurement, in *Dynamics of Fractal Surfaces*, edited by F. Family and T. Vicsek, World Sci., River Edge, N.J., 1991.

Wichman, R. W., and P. H. Schultz, Sequence and mechanisms of deformation around the Hellas and Isidis impact basins on Mars, *J. Geophys. Res.*, *94*, 17,333–17,357, 1989.

Wu, S. S. C., Topographic maps of the polar, western, and eastern regions of Mars, scale 1:15,000,000, *U.S. Geol. Surv. Map I-2160*, 1991.

Zuber, M. T., D. E. Smith, S. C. Solomon, D. O. Muhleman, J. W. Head, J. B. Garvin, J. B. Abshire, and J. L. Bufton, The Mars Observer Laser Altimeter investigation, *J. Geophys. Res.*, *97*, 7781–7797, 1992.

Zuber, M. T., L. Lim, and H. J. Zwally, The role of viscous deformation in the morphology of the Martian north polar cap, in *First International Conference on Mars Polar Science and Exploration*, edited by S. Clifford, D. Fisher, and J. Rice, pp. 45–46, Lunar and Planet. Inst., Houston, Tex., 1998a.

Zuber, M. T., et al., Observations of the north polar region of Mars from the Mars Orbiter Laser Altimeter, *Science*, *282*, 2053–2060, 1998b.

Zuber, M. T., et al., Internal structure and early thermal evolution of Mars from Mars Global Surveyor topography and gravity, *Science*, *287*, 1788–1793, 2000.

Zwally, H. J., A. Fountain, J. Kargel, L. Kouvaris, K. Lewis, D. MacAyeal, T. Pfeffer, and J. L. Saba, Morphology of Mars North Polar Cap, in *Second International Conference on Mars Polar Science and Exploration*, edited by S. Clifford, D. Fisher, and J. Rice, Lunar and Planet. Inst., Houston, Tex., 2000.

O. Aharonson, D. H. Rothman, and M. T. Zuber, Department of Earth, Atmospheric and Planetary Sciences, Massachusetts Institute of Technology, Cambridge, MA 02139 (oded@mit.edu)

(Received September 27, 2000; revised February 21, 2001; accepted March 12, 2001.)